Journal of the European Ceramic Society 41 (2021) 2617–2624

Contents lists available at ScienceDirect

Journal of the European Ceramic Society

journal homepage: www.elsevier.com/locate/jeurceramsoc

Original Article

Thin film growth effects on electrical conductivity in entropy stabilized oxides

V. Jacobson [a,b], D. Diercks [b], B. To [a], A. Zakutayev [a], G. Brennecka [b,*]

[a] National Renewable Energy Laboratory, 16000 Denver West Parkway, Golden, CO, United States
[b] Colorado School of Mines, 1500 Illinois Ave., Golden, CO, United States

ARTICLE INFO

Keywords:
Entropy
Oxide
Phase
Electrical Conductivity
Thin film

ABSTRACT

Entropy stabilization has garnered significant attention as a new approach to designing novel materials. Much of the work in this area has focused on bulk ceramic processing, leaving entropy-stabilized thin films relatively under-explored. Following an extensive multi-variable investigation of polycrystalline $(Mg_{0.2}Co_{0.2}Ni_{0.2}Cu_{0.2}Zn_{0.2})O$ thin films deposited via pulsed laser deposition (PLD), it is shown here that substrate temperature and deposition pressure have strong and repeatable effects on film texture and lattice parameter. Further analysis shows that films deposited at lower temperatures and under lower oxygen chamber pressure are ~40× less electrically resistive than otherwise identical films grown at higher temperature and pressure. Annealing these films in an oxygen-rich environment increases their electrical resistivity to match that of the films grown at higher temperatures and pressures. Because of this, the electric conductivity is hypothesized to be the result of polaron hopping mediated by transition metal valence changes which compensate for oxygen off-stoichiometry.

1. Introduction

High entropy alloys are a well-established field of work with applications in metallic property optimization [1–3]. In 2015, entropy stabilization was first applied to ceramic oxides [4,5], and a five cation material system, $(Mg_{0.2}Co_{0.2}Ni_{0.2}Cu_{0.2}Zn_{0.2})O$, was found to crystallize reversibly into a uniform rock salt structure when heated to a sufficiently high temperature (>875 °C for the equimolar composition); when quenched to room temperature, the material system retains the rock salt structure. Cation distribution within the entropy stabilized rock salt structure has been shown to be truly random and homogeneous over long range, with some local distortions in the oxygen anion sublattice in order to accommodate the different cation sizes [6] in addition to Jahn–Teller distortions [7–10] (Fig. 1). This entropy stabilized oxide has been the focus of many studies, and versions of it have been reported to work well as a Li-ion conductor [11] and anode for Li-ion batteries [12,13], and redox material for thermochemical water splitting [14]. Extremely high dielectric constants have also been reported [15]. Other high entropy ceramics have been found to work well as wear resistant coatings and thermal protection [16], as high performance thermoelectrics and ultrahigh temperature coatings [17,13]. It has also been established that high entropy ceramics, in contrast to high entropy alloys, are typically semicondutors or insulators with a band gap, making them interesting as functional materials. The world of high entropy ceramics extends beyond rock salt oxides and covers a broad structural spectrum, including rock salt, perovskite, fluorite, spinel, zinc blende, and half-Heusler structures [18]. This investigation is focused on the original high entropy ceramic oxide $(Mg_{0.2}Co_{0.2}Ni_{0.2}Cu_{0.2}Zn_{0.2})O$ in the rock salt structure. The majority of the prior rock salt $(Mg_{0.2}Co_{0.2}Ni_{0.2}Cu_{0.2}Zn_{0.2})O$ studies have been carried out on samples processed as bulk ceramics [19,4,15,9,17,13]; thin film studies are less common. The seminal work on these oxides [5] showed an inverse relationship between both pO_2 and substrate temperature on out-of-plane tetragonal lattice parameter in epitaxial thin films of $(Mg_{0.2}Co_{0.2}Ni_{0.2}Cu_{0.2}Zn_{0.2})O$. Another thin film study used pulsed laser deposition (PLD) to show that entropy stabilized thin films of $(Mg_{0.25(1-x)}Co_xNi_{0.25(1-x)}Cu_{0.25(1-x)}Zn_{0.25(1-x)})O$ can be tailored to engineer long range magnetic order and show promise for enhanced exchange coupling [20]. PLD has also been used to explore structural stability of the $(Mg_xNi_xCo_xCu_xZn_xSc_x)O$ $(x \approx 0.167)$ system as a function of growth parameters [21]. Depositing films using high-energy methods like PLD provides access to much higher effective

* Corresponding author.
E-mail address: gbrennec@mines.edu (G. Brennecka).

https://doi.org/10.1016/j.jeurceramsoc.2020.12.021
Received 26 June 2020; Received in revised form 3 December 2020; Accepted 9 December 2020
Available online 20 December 2020

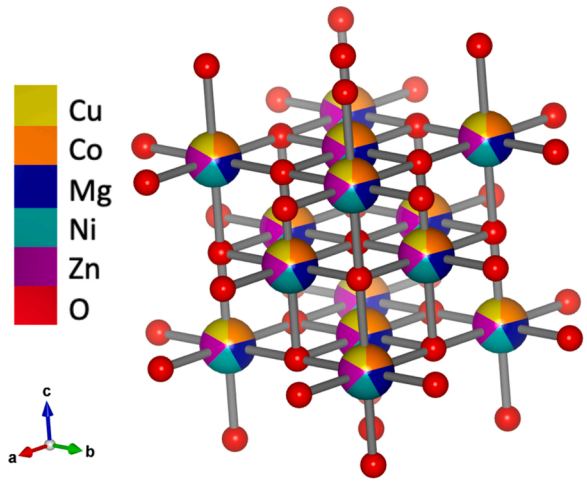

Fig. 1. The films in this study exhibit a rock salt crystal structure in which all five cations are randomly distributed on the cation sublattice with oxygen ions filling the anion sublattice.

temperatures (on the order of 30,000 K) than bulk processing allows. Note that the term "effective temperature" is used here to describe the estimated temperatures of the plasma generated by laser ablation and not as a measure of cation disorder [22], as cations are presumably fully disordered in this material system. In the current study, PLD is used to fabricate non-epitaxial chemically uniform single phase rock salt thin films of $(Mg_{0.2}Co_{0.2}Ni_{0.2}Cu_{0.2}Zn_{0.2})O$ on non-lattice matched substrates. Changing substrate temperature and chamber oxygen pressure enables tailoring of film texture, lattice parameter, and morphology as well as resulting through-thickness electrical resistivity. Varying deposition temperatures and pressures affects the growth of the deposited thin film, favoring (111) or (002) texture depending on these parameters, as well as compressing the lattice constant and changing morphology at lower deposition temperature. Electrical current density measurements through the thicknesses of the films indicate that a reduction in lattice constant is correlated with significantly lower electrical resistivity. Annealing these more conductive films in an oxygen rich environment causes the lattice constant to increase and the electrical resistivity to be increased by a factor of 20.

2. Experimental details

2.1. Targets

Stoichiometric $(Mg_{0.2}Co_{0.2}Ni_{0.2}Cu_{0.2}Zn_{0.2})O$ targets were fabricated by mixing equimolar amounts of MgO [Alfa Aesar, 99.99%], CoO [Alfa Aesar, 99.7%], NiO [Sigma Aldrich, 99.995%], CuO [Alfa Aesar, 99.995%], and ZnO [Alfa Aesar, 99.99%]. These were roller milled with Y-stabilized ZrO_2 milling media for 6 hours. The powder mix was pressed in a 1″ die to 80 MPa using a Carver hydraulic press without binder. Resulting pellets were sintered in air using the following profile: 5 °C/min ramp to 900 °C, hold 6 h, 10 °C/min ramp to 1100 °C, hold 8 h. After the 8 hour hold, each pellet was removed from the 1100 °C furnace and air quenched to room temperature. This sintering profile resulted in sufficiently dense (~87%) and uniform targets that were confirmed by x-ray diffraction to be polycrystalline single phase rock salt without preferential orientation (Fig. 2) [23]. A CuO target was fabricated by pressing and sintering 99.995% pure powder purchased from Alfa Aesar in a 1″ die to 80 MPa using a Carver hydraulic press without binder. The resulting pellet was sintered in air at 900 °C for 6 h with a ramp rate of 5 °C per minute. The resulting CuO target was approximately 88% dense. A PLD target of ZnO (99.9%) was purchased from Plasma Materials.

2.2. Pulsed laser deposition

Single phase films were deposited using a KrF (248 nm) excimer laser with pulse rates between 10 and 30 Hz and laser energies ranging from 100 to 350 mJ. Film structure was found to be rather insensitive to laser parameters, so a pulse rate of 20 Hz and laser energy of 200 mJ were selected as standard for continued study. Both Zn and Cu from the $(Mg_{0.2}Co_{0.2}Ni_{0.2}Cu_{0.2}Zn_{0.2})O$ target ablated in slightly lower concentrations than the other cations in the target (Zn approximately 1 at% lower, Cu approximately 6 at% lower), so separate CuO and ZnO targets were used to supplement depositions and grow stoichiometric films. Substrate temperature and chamber (oxygen) pressure combinations of 200, 300, or 450 °C and 50 or 100 mT were explored. The rest of this report focuses on samples deposited with a substrate temperature of 200 or 450 °C and oxygen pressure set to 50 or 100 mT; trends reported here are consistent across the rest of the deposition space. Substrates used in this study were borosilicate [Eagle2000] glass (EXG) and Pilkington NSG TEC 15 Glass with approximately 340 nm of fluorinated tin oxide coating (FTO, 13–15 Ω/sq).

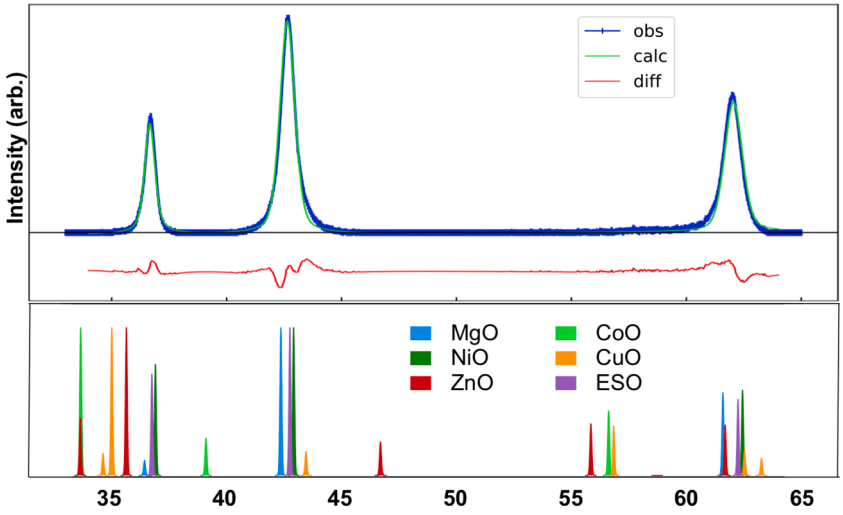

Fig. 2. XRD data with a Rietveld refinement confirms the polycrystalline cubic rock salt structure of the $(Mg_{0.2}Co_{0.2}Ni_{0.2}Cu_{0.2}Zn_{0.2})O$ PLD target with a lattice constant of 4.24 Å. In the above figure, "obs" is the observed data, "calc" is the calculated fit from the refinement, and "diff" shows the difference between observed and calculated data. The five precursor oxide reference patterns [24–28] are also shown to confirm that no residual precursor phases are observed.

Table 1
Average cation concentration from 44 points across each sample per XRF.

Sample type	Co (at%)	Ni (at%)	Cu (at%)	Zn (at%)	Mg (at%)
HTLP	26 ± 0.4	25 ± 0.4	23 ± 0.4	25 ± 0.4	–
HTHP	26 ± 0.5	24 ± 0.5	23 ± 0.5	26 ± 0.5	–
LTLP	25 ± 0.4	25 ± 0.5	23 ± 0.5	26 ± 0.4	–

2.3. Sample characterization

Samples were characterized using a variety of methods to validate their structure and composition before analyzing properties. Each thin film was measured in 44 different locations in order to confirm consistency of the film across the 2″ × 2″ substrate. Crystal structure and phase purity of both PLD targets and the resulting films were confirmed using a Bruker D8 Discover with Cu-k_α radiation. XRD data for several films were also collected at the Stanford Linear Accelerator on Beamline 1–5 (measurements were calibrated with a LaB_6 standard, however BL 1–5 does not correct for tilt of sample. Data presented here are measured to be approximately 0.08 Q low). Composition and thickness are confirmed using a Fischer XUV X-ray fluorescence tool (XRF); thickness varies radially from the plume center to the edges, which are 12% thinner. Compositional variance for each measured cation is less than 0.5 at% but is not associated with plume position, as substrates were rotated during deposition. In addition, energy dispersive spectroscopy (EDS) data were collected using an FEI Talos F200X transmission electron microscope (TEM), which was also used for bright field and high angle annular dark field imaging. Top electrical contacts with an area of 0.007 cm^2 were deposited through a shadow mask using a Temescal FC2000 e-beam tool, with 10 nm of Ti and 50 nm of Pt. Current density measurements were collected using a Keithley 2400 source meter under electric fields from 0 to ±67,000 or ±30,000 V/cm. Multiple measurements across the entire 2″ × 2″ sample were performed using a tungsten probe with a diameter of 0.4 mm to map the entire sample, as controlled by LabView.

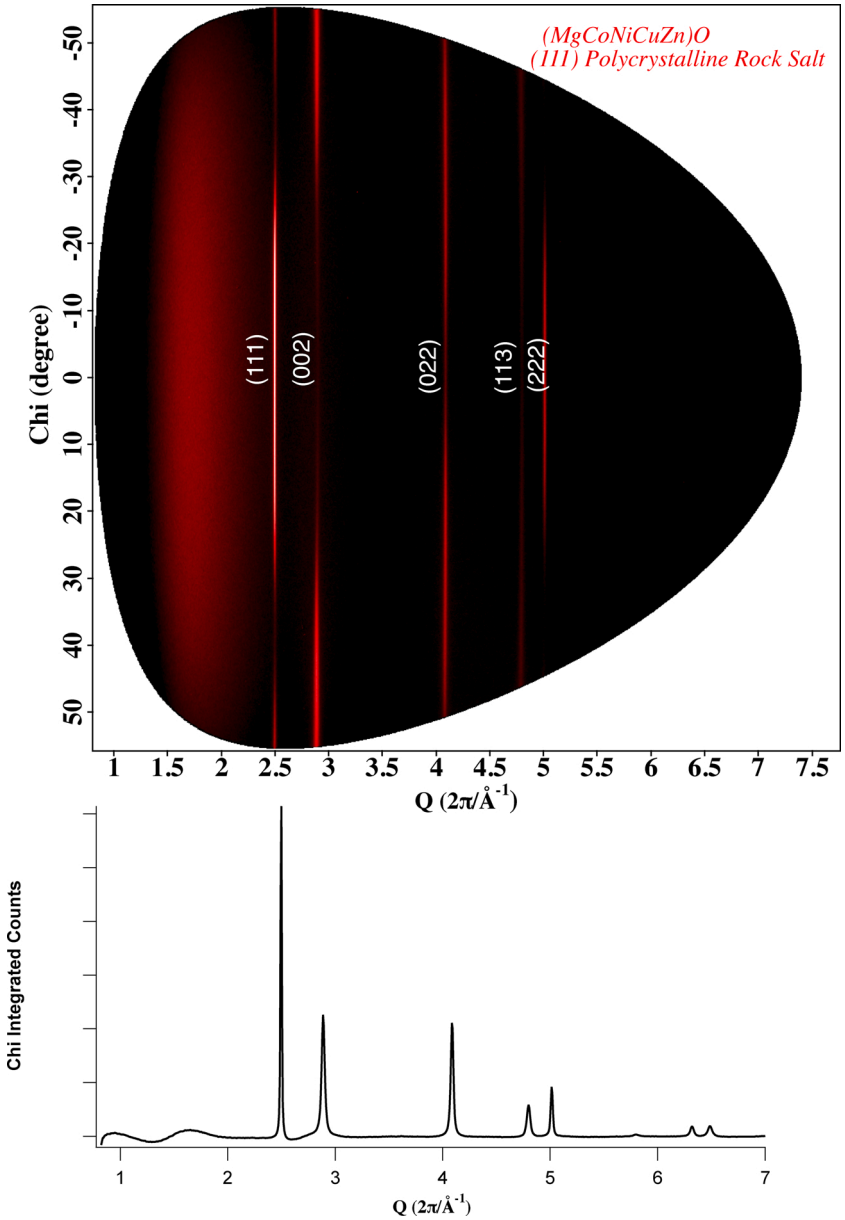

Fig. 3. Top: High resolution XRD data collected at SLAC on BL 1–5 show the (111)-textured polycrystalline growth of a cubic rock salt with moderate (111) crystallographic texture on a borosilicate glass substrate. **Bottom:** Integrated counts across approximately 4 degrees through the center of the measured Chi emphasize the (111) texture of the sample.

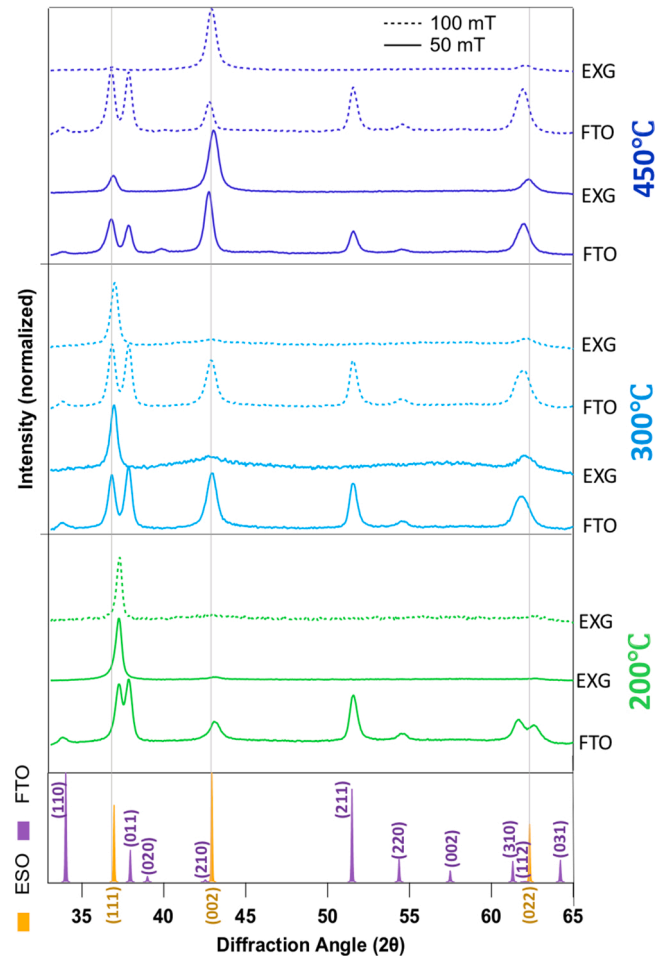

Fig. 4. Crystallographic texturing was found to change as a result of deposition temperature and partial pressure of oxygen. Overall, samples grown at 450 °C have a tendency to grow with an (002) texture when grown on either EXG or FTO substrates and at both 50 and 100 mT pO_2. Samples grown at 300 °C show (111) texturing at both 50 and 100 mT and on either EXG or FTO substrates. Samples grown at 200 °C with 50 or 100 mT all show (111) texturing along with peaks at higher 2θ, indicating a shorter lattice constant for these films. Samples grown on EXG glass versus FTO-coated glass are designated by "EXG" and "FTO".

Measurements were performed multiple times in series to verify repeatability and consistency, all using DC applied voltages. Plane view images of film microstructure were taken with an FEI Nova 630 SEM, while the cross sections were imaged using a Hitachi 4800 SEM. Several samples were annealed for 1 h at 300 °C under 520 torr of flowing oxygen in order to understand the effects of oxygen incorporation. The open-source COMBIgor package for commercial Igor Pro [29] was used for data analysis and visualization.

3. Results and discussion

3.1. Crystal structure

Arrays of XRF measurements (Table 1) confirm that cations are homogeneously distributed in these thin films, at least on a mesoscopic scale. On average, samples are all slightly lower in Cu than other measurable cations; Mg could not be measured using XRF because its atomic mass is too low for the instrument to identify. The slightly lower amounts of Cu do not alter the structure and are consistent across all depositions, so it does not appear to be the cause for the property trends reported here. XRD confirms that the rock salt structure of the films matches that of the desired rock salt ESO ($Mg_{0.2}Co_{0.2}Ni_{0.2}Cu_{0.2}Zn_{0.2}$)O (Fig. 3), similar to the target (Fig. 2), and suggests that all constituent cations are most likely randomly and homogeneously dispersed throughout the cation FCC sublattice [6,5]. Films grown on EXG at 200 °C under 50 mT pO_2 exhibit moderate levels of texturing in the (111) growth direction (Fig. 3) where the cubic lattice constant a is 4.23 Å. It is interesting to note the difference in the thin film lattice constant with that of the ($Mg_{0.2}Co_{0.2}Ni_{0.2}Cu_{0.2}Zn_{0.2}$)O target (4.24 Å), indicating that the thin film growth on an amorphous substrate exhibits some lattice compression in all directions compared to the target material.

Fig. 4 shows changes in film texture with substrate temperature and chamber pressure of oxygen. Note that all of the lattice constants for samples shown here are smaller than that of the bulk ESO target lattice constant (4.24 Å, Fig. 2). The samples in this study do not show the specific out of plane lattice compression identified in previous work on this material system [5] because the films here are not epitaxially constrained by the substrates and they are polycrystalline. They all show cubic compression where both the a and c lattice constants are slightly compressed relative to the bulk ceramic in equal amounts.

Three distinct growth types have been identified based on texture and lattice constant and will be the focus for the remainder of this paper.

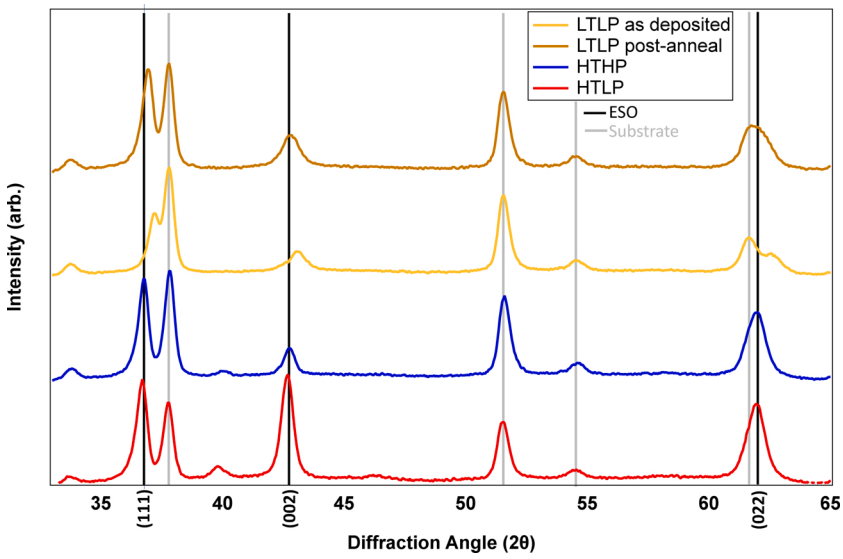

Fig. 5. Two dimensional XRD data collected using a Bruker D8 Discover show the lattice shift in the ESO rock salt peaks relative to the FTO peaks for Lower Temperature Lower Pressure (LTLP), Higher Temperature Higher Pressure (HTHP), and Higher Temperature Lower Pressure (HTLP). ESO peaks are identified by black lines and FTO peaks by grey lines. The LTLP as deposited samples show a shift to higher 2θ for ESO peaks, verifying a smaller lattice constant, while the LTLP post-anneal samples show a shift back to slightly lower 2θ, indicating lattice expansion in the anneal process.

Table 2
Summary of growth conditions and characteristics for all samples grown on FTO substrates and compared to previous works. *Note: LF and microstructure information for previous works have been approximated based on data provided in articles.

Sample type	Pressure (mT PO_2)	Temperature (°C)	Crystal texture	Lattice constant (Å)	Lotgering factor	Average lattice compression (%)	Microstructure	Resistance (kΩ cm)
HTLP	100	450	(002)	4.23	31%	0.31 ± 0.07	Columnar	3400 ± 175
HTHP	50	450	(111)	4.23	42%	0.20 ± 0.03	Columnar	1200 ± 50
LTLP	50	200	(111)	4.19	55%	1.37 ± 0.02	Random	51 ± 0.65
LTLP annealed	520k – annealed	300 – annealed	(111)	4.21	56%	0.71		1037 ± 50
Bulk Polyxtal [15]	–	1000	N/A	4.24	0%	1.86	Random	5000
Nanoparticles [12]	–	1000	N/A	a=4.17; c=4.2	0%	2.33	Random	–
MgO(001) epi [20]	50	300	(002)	4.15	100%	3.49	Epitaxial	–
TF on Al_2O_3 [5]	50	500	N/A	4.25	0%	1.16	Random	–

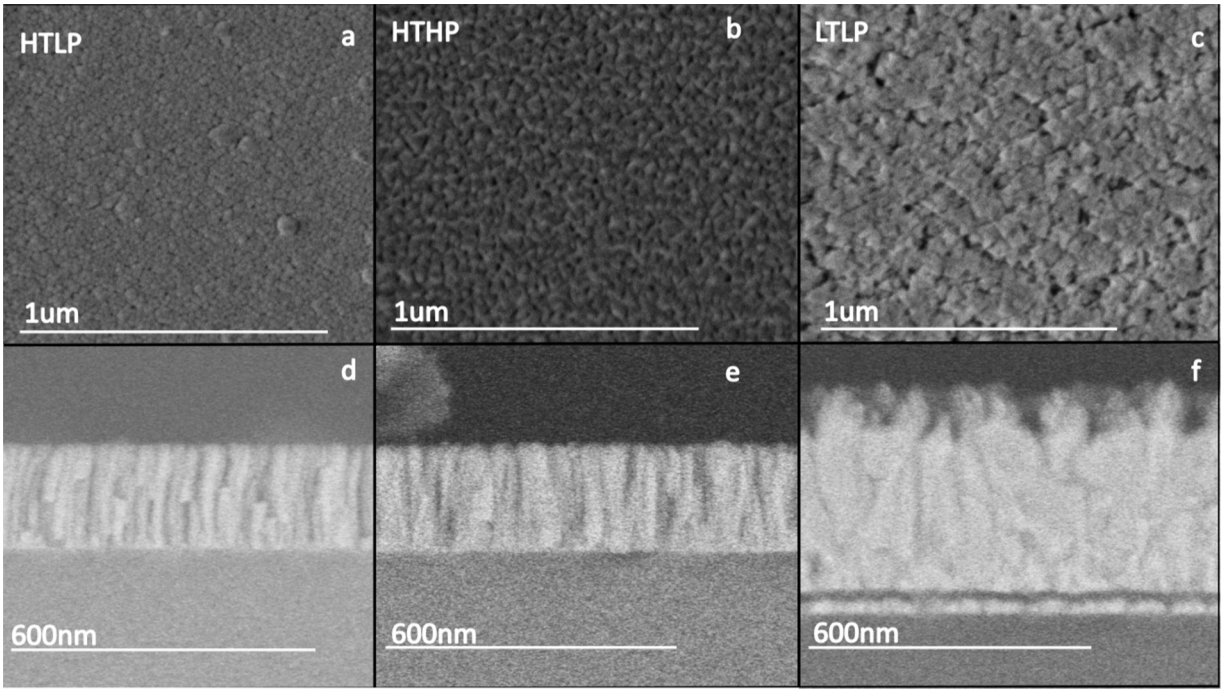

Fig. 6. HTLP and HTHP samples were imaged on bare glass substrates, LTLP were imaged on FTO-coated glass substrates. **(a–c)** SEM shows different surface morphologies for each of the three crystallographic orientations. **(d–f)** Cross-sectional SEM shows that the HTLP and HTHP samples have a fairly columnar grain structure, while the LTLP textured samples have overlapping grains and less uniformity across the film thickness. The additional layer in **f** shows the FTO layer beneath the ESO film. *Note: LTLP films were grown with 30% more laser pulses, making them thicker, as seen above in **f**.

These are shown in Fig. 5. Each of these three types of films is grown on FTO substrates and will be referred to as "HTHP" (Higher Temperature, Higher Pressure), "LTLP" (Lower Temperature, Lower Pressure), and "HTLP" (Higher Temperature, Lower Pressure) and are defined as follows: HTHP and HTLP both have a lattice constant of 4.23 Å while LTLP samples have a lattice constant of 4.19 Å. LTLP samples were also annealed in an oxygen-rich atmosphere, which resulted in an increase in their lattice constant to 4.21 Å. The Lotgering Factor [30,31] is used here to quantify the degree of crystallographic texturing; LF = 0% is purely random, LF = 100% is perfectly textured. All LF values in this paper were calculated from an integration across 4 degrees of Chi from a 2D detector. Films designated as "HTHP" show a (111) texture with an LF = 42% and are grown at 100 mT pO_2 and 450 °C; "HTLP" films show (002) texture with an LF = 31% and are grown at 50 mT pO_2 and 450 °C; "LTLP as-deposited" films show (111) texturing as well, but have an LF = 55% and are grown at 50 mT pO_2 and 200 °C; "LTLP post-anneal" films retain (111) texture with an LF = 56% and are annealed at 300 °C under 520 torr of flowing oxygen. This information is summarized in Table 2.

The definition for lattice strain [32] is $\frac{(c-c_{bulk})}{c_{bulk}}$, where c is the out-of-plane lattice constant and c_{bulk} is the bulk lattice constant associated with strain-free polycrystalline growth (here we use the lattice constant from the ESO target of 4.24 Å as the bulk value). We can apply this model to ESO data as a way to quantify the degree of compression happening in these films relative to bulk samples. The comparative lattice constant for individual thin film samples is calculated for a cubic crystal lattice and derived from individual XRD scans using the 2θ positions of the center of at least two peaks from different crystal plane families ((111) and (002)). The lattice shrinkage for LTLP samples indicates some fundamental difference in these samples from the HTHP and HTLP samples. All LTLP samples grown on FTO have an isotropic compression greater than 1.3%, while HTLP and HTHP samples have an isotropic compression no greater than 0.3%. Annealed LTLP samples have an isotropic lattice compression of 0.71%.

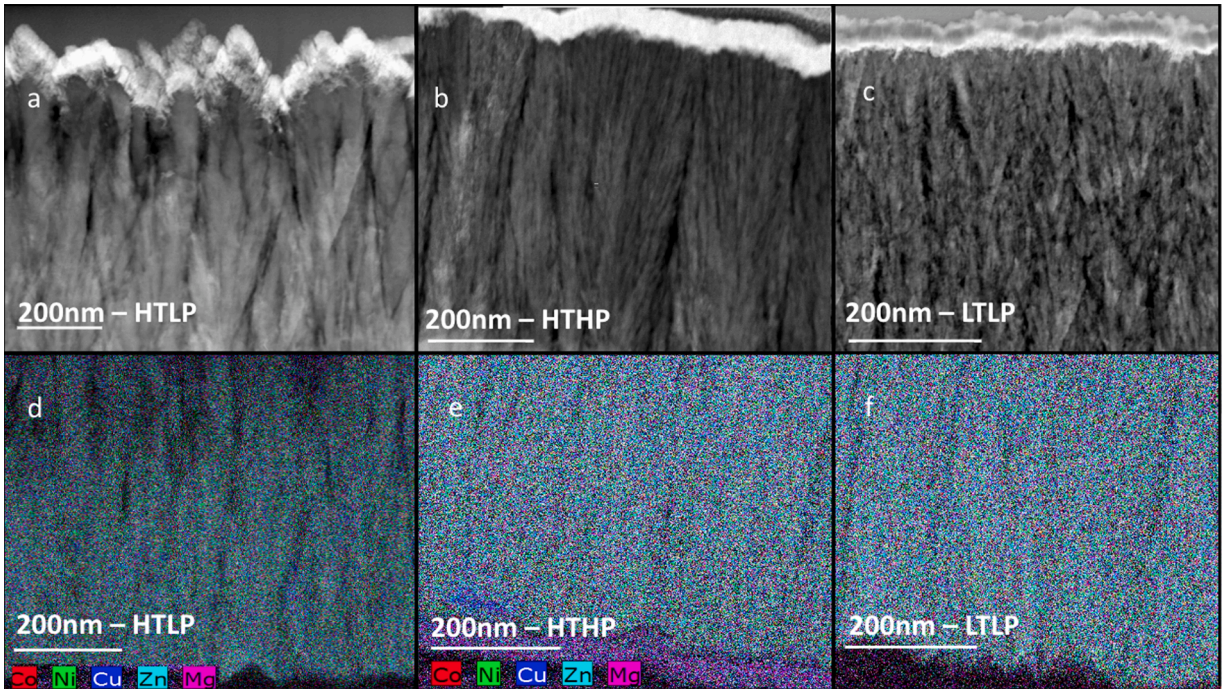

Fig. 7. Film microstructure as shown in HAADF images is consistent with columnar grains seen in SEM. **(a)** Samples with an HTLP texture show a higher degree of surface roughness in addition to a lower degree of collimation than in the HTHP samples but a higher degree of collimation than the LTLP samples. **(b)** HTHP samples show a high degree of collimation in grain structure, **(c)** LTLP samples show grains to be less ordered than in the HTHP and HTLP samples. **(d–f)** Cation distributions for all three types of crystallographic texturing are uniform and homogeneous as shown by EDS mapping.

3.2. Microstructure

SEM images revealed notably different microstructures among these three growth types. The HTLP textured samples, grown at 450 °C and 50 mT O_2, have almost circular grains growing in a largely columnar fashion, as seen in Fig. 6a,d. HTHP samples, grown at 450 °C and 100 mT O_2, also show columnar grains, however these grains exhibit a triangular shape at the surface consistent with the cube corners of a (111)-textured rock salt, shown in Fig. 6b and e. LTLP samples, grown at 200 °C and 50 mT O_2, do not exhibit columnar growth, and grains show no consistent morphology, seen in Fig. 6c and f. It is not unusual for films grown at higher temperatures to exhibit more regular columnar growth as the higher substrate temperature provides additional mobility for atoms to settle into a somewhat lower energy configuration before being fully "quenched" [33]. The HTHP films are grown under a higher partial pressure of oxygen and higher substrate temperature. Higher pressure leads to more oxidizing conditions during growth, while the higher temperature leads to more reducing conditions according to the ideal gas law [34], but also may give the material the kinetic energy needed to incorporate oxygen into the lattice [5]. The kinetic limitations of the lower substrate temperature coupled with a lower growth pO_2 suggest that oxygen incorporation into the lattice may be different in such samples, leading to different oxygen off-stoichiometry.

Uniformity of the cation distributions is shown with an EDS map across a HAADF image in Fig. 7. The microstructures and z-contrast seen in Fig. 7 are consistent throughout the thickness of each film. A TEM and atom probe tomography study on bulk samples of the same composition [35] showed that annealing could lead to Cu segregation, but no evidence of such segregation is observed here.

It has been established [5] that phase decomposition of bulk samples begins in an annealing process around 600 °C, which may suggest some likelihood of phase segregation for film samples grown at higher temperatures. Such segregation is accompanied by XRD peak broadening [9]. Films in this study exhibit consistent full width half maximum values for XRD peaks across all deposition temperatures (Fig. 8). Thus, neither XRD nor TEM (imaging and EDS) show any evidence of cation segregation in these films.

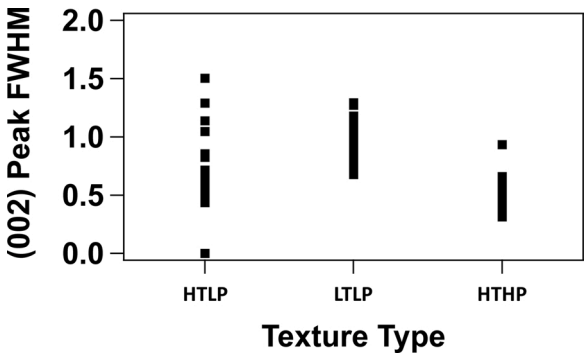

Fig. 8. None of the three sample types show a shift in XRD data FWHM calculations, indicating that cation segregation at higher temperatures is unlikely to be the underlying cause of the observed differences in resistance.

3.3. Electrical properties

Films of approximately 1 μm thickness were grown on FTO coated borosilicate glass to enable through-thickness current density measurements. Measuring the resistivity of these films as a function of applied voltage reveals different electrical behavior for the LTLP samples from the other two types of films. Annealing the LTLP films in oxygen changed their resistive properties to be more closely matched with those of the HTHP and HTLP samples. Measurements collected on HTLP samples reveal a nonlinear resistivity on the order of 3.42 ± 0.175 MΩ cm. HTHP samples show a nonlinear resistivity on the order of 1.2 ± 0.05 MΩ cm. LTLP samples are much less resistive, with an average measured resistivity of 51 ± 0.65 kΩ cm. Annealed LTLP samples have a measured resistivity of 1.04 MΩ cm. The comparison of this data can be seen in

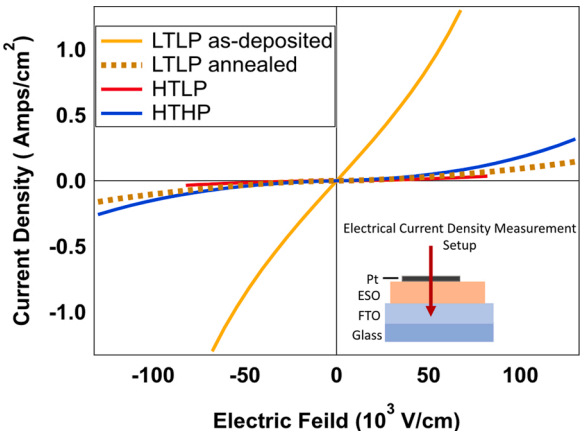

Fig. 9. The resistance of HTLP and HTHP samples is much higher than in the LTLP textured samples. Reported values are an average of at least 30 measurements for each sample type. LTLP samples that have been annealed under oxygen exhibit more resistive behavior, on the same order as the HTHP and HTLP samples, indicating that oxygen added to the system combined with a low temperature anneal results in higher resistivity. Inset: Schematic of measurement configuration.

Fig. 9.

The nonlinearity was initially hypothesized to be a result of self-heating of the sample during the measurement. In order to rule this out, a series of experiments was run to determine the effects of repeated measurements on the same sample and therefore the effects of self-heating. One measurement was collected with current flowing through the sample for approximately 200 seconds, and another set of twenty rapidly repeated measurements was run with one immediately following the other. The first and last measurements were compared with each other and with the 200 second measurement. Neither of these measurements was appreciably different from one another, nor did they differ from the single measurements collected and presented here. Based on this series of repeated current density measurements over a range of different frequencies and duration, it is unlikely that self-heating is the cause of the nonlinearity because the measurements proved consistent across all acquisition timing parameters. It should be noted that the electrical contacts in our measurement stack are likely imperfectly ohmic contacts, which may explain some of the nonlinearity in the data.

Samples deposited at the lowest substrate temperature (200 °C) and lowest oxygen pressure (50 mT) were the least electrically resistive. Because these films were grown at the lowest substrate temperature, they are the most kinetically limited sample set [5]. EDX data collected and shown in Fig. 7 confirm a homogeneous distribution of cations, supporting the hypothesis that the variation in electrical response between these three types of samples arises from something other than cation segregation. It was hypothesized that these films were oxygen-deficient, which could be compensated for by a change in average cation valence, consistent with the increased conductivity. In order to explore this idea further, LTLP samples were annealed in an oxygen-rich atmosphere and characterized again using XRD and current density measurements in order to understand the effects of adding oxygen to the LTLP system. This data shows that a short, low temperature anneal in an oxygen-rich environment is sufficient to cause an increase in electrical resistivity by a factor of 20, approaching the resistivity of the HTHP and HTLP samples (Fig. 9). Annealed LTLP samples also showed an increase in the lattice constant to 4.21 Å as seen in Fig. 5.

In this case, the most likely mechanism of electrical conductivity is polaron hopping; the hopping distance is shorter for polarons in the compressed lattice, making the hop more likely to occur and decreasing electrical resistivity [36,37]. Previous studies have also found that low temperature depositions tend to shift Co^{2+} to Co^{3+} and cause lattice contraction [10]. These results are consistent with the XRD and electrical data presented here and allude to the likelihood of cation valence as a major contributor to conduction mechanisms. There is also a clear correlation between lower electrical resistivity (Fig. 9) and non-columnar microstructure (Fig. 6), but the exact origin of this correlation is not clear. The results presented here are consistent with previously published data as represented by Table 2. One publication has reported electrical resistivity [15] in bulk samples to be 5 MΩ cm, which is consistent with the more resistive measurements in the present study. Presumably, the bulk samples from this previous publication [15] also have a random microstructure similar to that of the LTLP samples, but the improved density of a thin film over a bulk processed sample would decrease electrical resistivity and explain the lower resistance values measured in our thin film samples. Other publications do not present resistivity data, however they do show a consistent lattice constant across non-epitaxial samples. The epitaxial samples grown on $MgO_{(001)}$ substrates are reported to have a much smaller lattice constant (4.15 Å). Nanopowder samples show some tetragonal distortion not seen in other bulk studies.

4. Conclusions

Single phase rock salt $(Mg_{0.2}Co_{0.2}Ni_{0.2}Cu_{0.2}Zn_{0.2})O$ samples can be deposited efficiently using PLD, and temperature and partial pressure of oxygen can be used to control crystallographic texturing. Thin film samples grown on FTO with a lattice constant of 4.23 Å and either (111) or (002) texturing (HTHP or HTLP, respectively) demonstrate a nonlinear electrical resistance between 1 and 3.4 MΩ cm, while (111) textured films with a lattice constant of 4.19 Å (LTLP) are significantly more conductive, with resistivity values on the order of 50 kΩ cm. When these LTLP samples are annealed in an oxygen rich environment, their lattice constant increases to 4.21 Å and their resistivity increases to match that of the HTHP and HTLP samples. The increased resistivity of oxygen-annealed LTLP samples indicates that an oxygen deficiency is the likely cause of the lower resistivity in the as-deposited LTLP samples. The primary difference in microstructure for resistive versus conductive films is that the conductive films have a more random grain structure with nucleation occurring throughout the films, and the resistive films show columnar grains with nucleation occurring primarily at the substrate. The smaller lattice constant also indicates a shorter hopping distance for any induced charge in the material system. This, coupled with a likely oxygen off-stoichiometry during growth, makes polaron hopping a likely candidate for the conduction mechanism. Ultimately, this work indicates that thin film samples grown on FTO at 50mT pO_2 and a substrate temperature of 200 °C are less electrically resistive than samples grown at higher substrate temperatures with a more organized microstructure by a factor of forty, likely as a result of an oxygen deficiency. The data presented here are consistent with previous reports on this material.

Declaration of Competing Interest

The authors report no declarations of interest.

Acknowledgements

This work was authored in part by the National Renewable Energy Laboratory (NREL), operated by Alliance for Sustainable Energy LLC, for the U.S. Department of Energy (DOE) under contract no. DE-AC36-08GO28308. Work at NREL by A.Z. was funded by the Office of Energy Efficiency and Renewable Energy (EERE), under Hydrogen and Fuel Cell Technologies Office (HFTO), as a part of HydroGEN Energy Materials Network (EMN) consortium. Work at CSM by G.B. and V.J. was partially supported by the National Science Foundation (DMR-1555015 andDMREF-1534503). The use of Stanford's Synchrotron Radiation Lightsource, SLAC National Accelerator Laboratory, was

supported by DOE-SC-BES under Contract No. DE-AC02-76SF00515. We would like to thank K. Talley and A. Mis for assistance in data processing with COMBIgor; P. Walker for helping to streamline the FIB liftout process; K. Gann for technical support; A. Mehta and M.S. Perera for support on SLAC's BL 1-5; B. Gorman for TEM guidance. The views expressed in the article do not necessarily represent the views of the DOE or the U.S. Government.

References

[1] B. Cantor, I. Chang, P. Knight, A. Vincent, Microstructural development in equiatomic multicomponent alloys, Mater. Sci. Eng. A 375-377 (1–2 SPEC. ISS) (2004) 213–218, https://doi.org/10.1016/j.msea.2003.10.257.
[2] B. Gludovatz, A. Hohenwarter, D. Catoor, E. Chang, E. George, R. Ritchie, A fracture-resistant high-entropy alloy for cryogenic applications, Science 345 (6201) (2014) 1153–1158, https://doi.org/10.1126/science.1254581.
[3] A. Gali, E. George, Tensile properties of high- and medium-entropy alloys, Intermetallics 39 (2013) 74–78, https://doi.org/10.1016/j.intermet.2013.03.018.
[4] C.M. Rost, E. Sachet, T. Borman, A. Moballegh, E. Dickey, D. Hou, J. Jones, S. Curtarolo, J. Maria, Entropy-stabilized oxides, Nat.Commun. 6 (2015) 8485, https://doi.org/10.1038/ncomms9485.
[5] C.M. Rost, Entropy-Stabilized Oxides: Explorations of a Novel Class of Multicomponent Materials (Ph.D. thesis), North Carolina State University, 2016.
[6] C. Rost, Z. Rak, D. Brenner, J. Maria, Local structure of the mgxnixcoxcuxznxo ($x=0.2_{xxxxx}x = 0.2$ entropy-stabilized oxide: An exafs study, J. Am. Cer. Soc. 100 (6) (2017) 2732–2738, https://doi.org/10.1111/jace.14756.
[7] L.K. Bhaskar, V. Nallathambi, R. Kumar, Critical role of cationic local stresses on the stabilization of entropy-stabilized transition metal oxides, J. Am. Ceram. Soc. 103 (5) (2020) 3416–3424, https://doi.org/10.1111/jace.17029.
[8] Z. Rák, J.P. Maria, D.W. Brenner, Evidence for Jahn-Teller compression in the (Mg Co Ni Cu Zn)O entropy-stabilized oxide: a DFT study, Mater. Lett. 217 (2018) 300–303, https://doi.org/10.1016/j.matlet.2018.01.111.
[9] D. Berardan, A.K. Meena, S. Franger, C. Herrero, N. Dragoe, Controlled Jahn-teller distortion in (mgconicuzn)o-based high entropy oxides, J. Alloys Compds. 704 (2017) 693–700, https://doi.org/10.1016/j.jallcom.2017.02.070.
[10] P.B. Meisenheimer, L.D. Williams, S.H. Sung, J. Gim, P. Shafer, G.N. Kotsonis, J. P. Maria, M. Trassin, R. Hovden, E. Kioupakis, J.T. Heron, Magnetic frustration control through tunable stereochemically driven disorder in entropy-stabilized oxides, Phys. Rev. Mater. 3 (10) (2019) 1–9, https://doi.org/10.1103/PhysRevMaterials.3.104420.
[11] D. Bérardan, S. Franger, A. Meena, N. Dragoe, Room temperature lithium superionic conductivity in high entropy oxides, J. Mater. Chem. A 4 (24) (2016) 9536–9541, https://doi.org/10.1039/c6ta03249d.
[12] N. Qiu, H. Chen, Z. Yang, S. Sun, Y. Wang, Y. Cui, A high entropy oxide (mg0.2co0.2ni0.2cu0.2zn0.2o) with superior lithium storage performance, J. Alloys. Compds. 777 (2019) 767–774, https://doi.org/10.1016/j.jallcom.2018.11.049.
[13] A. Sarkar, Q. Wang, A. Schiele, M.R. Chellali, S.S. Bhattacharya, D. Wang, T. Brezesinski, H. Hahn, L. Velasco, B. Breitung, High-Entropy Oxides: fundamental Aspects and Electrochemical Properties, Adv. Mater. 31 (26) (2019), https://doi.org/10.1002/adma.201806236.
[14] S. Zhai, J. Rojas, N. Ahlborg, K. Lim, M.F. Toney, H. Jin, W.C. Chueh, A. Majumdar, The use of poly-cation oxides to lower the temperature of two-step thermochemical water splitting, Energy Environ. Sci. 11 (8) (2018) 2172–2178, https://doi.org/10.1039/c8ee00050f.
[15] D. Bérardan, S. Franger, D. Dragoe, A. Meena, N. Dragoe, Colossal dielectric constant in high entropy oxides, Phys. Stat. Sol. Rapid Res. Lett. 10 (4) (2016) 328–333, https://doi.org/10.1002/pssr.201600043.
[16] C. Oses, C. Toher, S. Curtarolo, High-entropy ceramics, Nat. Rev. Mater. 5 (4) (2020) 295–309, https://doi.org/10.1038/s41578-019-0170-8.
[17] D. Liu, X. Peng, J. Liu, L. Chen, Y. Yang, L. An, Ultrafast synthesis of entropy-stabilized oxide at room temperature, J. Eur. Ceram. Soc. 40 (6) (2020) 2504–2508, https://doi.org/10.1016/j.jeurceramsoc.2020.01.018.
[18] R.Z. Zhang, M.J. Reece, Review of high entropy ceramics: design, synthesis, structure and properties, J. Mater. Chem. A 7 (39) (2019) 22148–22162, https://doi.org/10.1039/c9ta05698j.
[19] Z. Rak, C. Rost, M. Lim, P. Sarker, C. Toher, S. Curtarolo, J. Maria, D. Brenner, Charge compensation and electrostatic transferability in three entropy-stabilized oxides: results from density functional theory calculations, J. Appl. Phys. 120 (9) (2016) 095015, https://doi.org/10.1063/1.4962135.
[20] P. Meisenheimer, T. Kratofil, J. Heron, Giant enhancement of exchange coupling in entropy-stabilized oxide heterostructures, Sci. Rep. 7 (1) (2017) 3–8, 110.1038/s41598-017-13810-5.
[21] G. Kotsonis, C. Rost, D. Harris, J. Maria, Epitaxial entropy-stabilized oxides: growth of chemically diverse phases via kinetic bombardment, MRS Commun. 8 (2018) 1371–1377, https://doi.org/10.1557/mrc.2018.184.
[22] P. Ndione, Y. Shi, V. Stevanovic, S. Lany, A. Zakutayev, P. Parilla, J. Perkins, J. Berry, D. Ginley, M. Toney, Control of the electrical properties in spinel oxides by manipulating the cation disorder, Adv. Funct. Mater. 24 (5) (2014) 610–618, https://doi.org/10.1002/adfm.201302535.
[23] B.H. Toby, R.B. Von Dreele, GSAS-II: the genesis of a modern open-source all purpose crystallography software package, J. Appl. Crystallogr. 2 (46) (2013) 544–549, https://doi.org/10.1107/S0021889813003531.
[24] V. Tsirelson, A. Avilov, Y. Abramov, E. Belokoneva, R. Kitaneh, D. Feil, X-ray and Electron Diffraction Study of Mgo, Acta. Cryst. B 54 (1) (1970) 8–17, https://doi.org/10.1107/S0108768197008963.
[25] M. Redman, E. Steward, Cobaltous oxide with the zinc blende/wurtzite-type crystal structure, Nature 193 (4818) (1962) 867, https://doi.org/10.1038/193867a0.
[26] L. Thomassen, An x-ray investigation of the system cr2o3-nio1, J. Am. Chem. Soc. 63 (5) (1940) 1134–1136, https://doi.org/10.1021/ja01862a037.
[27] S. Åsbrink, J. Norrby, A refinement of the crystal structure of copper(ii) oxide with a discussion of some exceptional e.s.d.'s, Acta Cryst. B 26 (1) (1970) 8–15, https://doi.org/10.1107/S0567740870001838.
[28] S. Abrahams, J. Bernstein, Remeasurement of the structure of hexagonal zno, Acta Cryst. B25 (1969) 1233–1236, https://doi.org/10.1107/S0567740869003876.
[29] K. Talley, S. Bauers, C. Melamed, M.C. Papac, K. Heinselman, I. Khan, D. Roberts, V. Jacobson, A. Mis, G. Brennecka, J. Perkins, A. Zakutayev, Combigor: data-analysis package for combinatorial materials science, ACS Combin. Sci. 21 (7) (2019) 537–547, https://doi.org/10.1021/acscombsci.9b00077.
[30] R. Furushima, S. Tanaka, Z. Kato, K. Uematsu, Orientation distribution-Lotgering factor relationship in a polycrystalline material – as an example of bismuth titanate prepared by a magnetic field, J. Ceram. Soc. Jpn. 118 (1382) (2010) 921–926, https://doi.org/10.2109/jcersj2.118.921.
[31] J. Jones, E. Slamovich, K. Bowman, Critical evaluation of the Lotgering degree of orientation texture indicator, J. Mater. Res. 19 (11) (2004) 3414–3422, https://doi.org/10.1557/JMR.2004.0440.
[32] H. Wei, M. Jenderka, M. Grundmann, M.L. M, Lanio3 films with tunable out-of-plane lattice parameter and their strain-related electrical properties, Phys. Stat. Sol. Appl. Mater. Sci. 212 (9) (2015) 1925–1930, https://doi.org/10.1002/pssa.201431695.
[33] A. Infortuna, A.S. Harvey, L.J. Gauckler, Microstructures of CGO and YSZ thin films by pulsed laser deposition, Adv. Funct. Mater. 18 (1) (2008) 127–135, https://doi.org/10.1002/adfm.200700136.
[34] J. Osorio-Guillén, S. Lany, S.V. Barabash, A. Zunger, Magnetism without magnetic ions: percolation, exchange, and formation energies of magnetism-promoting intrinsic defects in CaO, Phys. Rev. Lett. 96 (10) (2006) 1–4, https://doi.org/10.1103/PhysRevLett.96.107203.
[35] D.R. Diercks, G.L. Brennecka, B.P. Gorman, C.M. Rost, J. Maria, Nanoscale compositional analysis of a thermally processed entropy-stabilized oxide via correlative tem and apt, Microsc. Microanal. 23 (2017) 1640–1641, https://doi.org/10.1017/S1431927617008868.
[36] M. Huda, A. Walsh, Y. Yan, S. Wei, M. Al-Jassim, Electronic, structural, and magnetic effects of 3d transition metals in hematite, J. Appl. Phys. 107 (12) (2010), https://doi.org/10.1063/1.3432736.
[37] A. Kleiman-Shwarsctein, M. Huda, A. Walsh, Y. Yan, G. Stuckyst, Y. Hu, M. Al-Jassim, E. McMland, Electrodeposited aluminum-doped a-fe2o3 photoelectrodes: experiment and theory, J. Appl. Phys. 22 (2) (2010) 510–517, https://doi.org/10.1021/cm903135j.